A comparison of straight-ray and curved-ray surface wave tomography approaches at near-surface studies

Mohammadkarim Karimpour[1], Evert Slob[2], Laura Valentina Socco[1]

[1]Politecnico di Torino, Turin, 10129, Italy
5 [2]Delft University of Technology, Delft, 2628 CN, Netherlands

Correspondence to: Mohammadkarim Karimpour (mohammadkarim.karimpour@polito.it)

Abstract. Surface waves are widely used to model shear-wave velocity of the subsurface. Surface wave tomography (SWT) has recently gained popularity for near-surface studies. Some researchers have used straight-ray SWT in which it is assumed that surface waves propagate along the straight line between receiver pairs. Alternatively, curved-ray SWT can be employed
10 by computing the exact paths between the receiver pairs. SWT is a well-established method in seismology and has been employed in numerous seismological studies. However, it is important to make a comparison between these two SWT approaches for near-surface applications since the amount of information and the level of complexity in near-surface are different from seismological studies. We apply straight-ray and curved-ray SWT to four near-surface examples and compare the results in terms of the quality of the final model and the computational cost.

1 Introduction

Surface waves are commonly analysed to build shear-wave velocity (VS) models. Surface wave tomography (SWT) is a well-established method in seismological studies, where numerous researchers have used it to construct subsurface velocity models at global and regional scale by inverting earthquake signals (Woodhouse and Dziewonski, 1984; Ekstrom et al., 1997; Ritzwoller and Levshin, 1998; Simons et al., 1999, Boschi and Ekstrom, 2002; Yao et al., 2010). Some authors have
20 applied SWT using ambient noise cross-correlation to retrieve regional crustal structures (Boschi and Dziewonski, 1999; Shapiro et al., 2004; Lin et al., 2008, Kästle et al., 2018).

SWT usually consists of three steps (Yoshizawa and Kennett, 2004; Yao et al., 2008). First, different path-averaged dispersion curves (DCs) are computed for different receiver pairs aligned with a source. Then, the DCs are inverted to build phase velocity maps at different period (frequency). Finally, the obtained phase velocity maps are inverted to produce 1D VS
25 models at different locations. However, the efficiency of SWT can be increased by the direct inversion of the path-averaged DCs, i.e., skipping the intermediate step of building phase velocity maps (Boschi and Ekstrom, 2002; Boiero, 2009; Fang et al., 2015).

Traditionally in seismology, SWT has been employed assuming great-circle propagation of surface waves (Trampert and Woodhouse, 1995; Ekstrom et al., 1997; Passier et al., 1997; Ritzwoller and Levshin, 1998; Boschi and Dziewonski, 1999;

30 van Heijst and Woodhouse, 1999; Simons et al., 1999; Boschi and Ekstrom, 2002; Lin et al., 2008; Yao et al., 2010; Bussat and Kugler, 2011; Kästle et al., 2018). However, some researchers have employed SWT not assuming the great-circle propagation of surface waves. Spetzler et al. (2002) carried out a synthetic experiment to study the effect of scattering in surface wave tomography. Yoshizawa and Kennet (2004) incorporated ray tracing and finite frequency effects to update the phase velocity maps. Trampert and Spetzler (2006) compared the obtained models from finite-frequency and ray theory

35 SWT. They concluded that since the choice of regularization affects the model significantly, the only way to increase the resolution of the model is to increase the data coverage. Bozdag and Trampert (2008) compared great-circle, exact ray and finite frequency approximations for crustal corrections and pointed out that common extensions to great-circle assumption (exact ray and finite frequency approximations) might not improve crustal corrections significantly. Gouédard et al. (2010) proposed eikonal tomography to build 2D phase velocity maps without a priori information.

40 In near-surface studies, the shot locations can be optimised to ensure that a high coverage of DCs can be achieved. This abundance of information facilitates shallow 2D or 3D characterization with great details. Due to its ability to provide high lateral resolution, SWT has recently attracted the attention of researchers for near-surface studies, where high lateral heterogeneity is expected. Few researchers have used SWT for near-surface characterization assuming straight ray propagation of surface waves: Kugler et al. (2007) characterized shallow-water marine sediments using Scholte waves

45 dispersion data, Picozzi et al. (2009) applied SWT on high-frequency seismic noise data to construct a VS model up to 25 m depth, Rector et al. (2015) employed SWT to obtain a VS model in a mining site, Ikeda and Tsuji (2020) successfully applied SWT in laterally heterogeneous media, Papadopoulou (2021) showed the applicability of SWT in near-surface characterization in a mining site consisting of hard rocks, Khosro Anjom (2021) constructed a 3D VS model applying SWT on a large 3D dataset acquired for testing purposes in a mining area.

50 Since the level of complexity and lateral heterogeneity in the near-surface is expected to be higher than in most seismological studies, the straight ray approximation of surface waves may not be valid and curved-ray tomography should be used by means of ray tracing at each frequency. Fang et al. (2015) applied SWT on a shallow crustal study considering the effect of heterogeneity on wave propagation. They performed surface wave ray tracing at each frequency using a fast-marching method (Rawlinson and Sambridge, 2004). Wu et al. (2018) applied curved-ray SWT to obtain a shallow VS

55 model at a mining site. Barone et al. (2021) applied different tomography methods, including eikonal tomography, to 3D active seismic data.

In curved-ray SWT, at each iteration a ray tracing method is applied at each frequency component to compute the ray path between the source and receivers. Even though this can increase the accuracy of the final model, it will lead to higher computational cost compared with straight-ray SWT. The computational efficiency is of great importance in seismic near-

60 surface since, compared to seismological studies, the abundance of data at active seismic near-surface projects can increase the computational cost significantly. Therefore, it is necessary investigate the gained improvement together with the associated additional computational cost from the curved-ray SWT over the straight-ray approach.

We apply straight- and curved-ray SWT on four datasets. Two examples include 3D synthetic models containing lateral velocity heterogeneity. We then apply SWT on two field datasets to evaluate the method on real data. For each dataset, 3D

65 VS models from straight- and curved-ray SWT are obtained, and the accuracy and computational efficiency of the two approaches are compared.

2 Method

The input data for SWT inversion are DCs. For a given array configuration, we optimise the locations of shots to ensure having high coverage DCs with minimum number of shots based on the guidelines by Da Col et al. (2020). To do that, many

70 shots are defined as a regular grid and for every shot the aligned receiver pairs are computed. Then, the shots providing the highest number of unique receiver pairs are picked for the acquisition. Once the acquisition layout is finalised, the DCs are estimated from the acquired data. A data-driven automatic picking two-station code is used to compute the path average slowness dispersion data between each receiver pair aligned with a source, and the DCs distorted by noise are discarded (for details see Papadopoulou, 2021). The subsurface is discretized into a set of 3D grid blocks where it is assumed that the only

75 unknown parameter of each grid block is the *VS* value while *VP* and density (ρ) are assumed to be known as a priori information. For every defined model point m_k, which consists of a vertical stack of grid blocks, the local phase slowness (p_k) for each frequency is computed using a Haskell (1953) and Thomson (1950) forward model modified by Dunkin (1965). To obtain the forward response in the curved-ray SWT, first the ray path between the receiver pair (R$_1$-R$_2$) for each frequency of the DC should be computed. Having computed the local 1D phase slownesses, the ray paths ($l_{R_1R_2}$) are obtained

80 by solving the eikonal equation using a finite-difference scheme proposed by Noble et al. (2014). Once the frequency dependent ray path between the receiver pair is calculated, the forward response (i.e., simulated DCs) is computed as:

$$p_{R_1R_2}(f) = \frac{\int_{l_{R_1R_2}} p(f,l)dl}{\int_{l_{R_1R_2}} dl} \; , \tag{1}$$

where $p_{R_1R_2}(f)$ represents the frequency dependent average phase slowness between the receiver pair. In the straight-ray SWT, the forward response (Eq. 1) is obtained with no need to compute the ray paths since the paths are already defined as

85 straight lines.

The employed inversion algorithm is based on the method proposed by Boiero (2009). We solve the inverse problem aiming at minimising the misfit function (Φ) which is defined as:

$$\Phi = \left[\left(\mathbf{d}_{obs} - g(\mathbf{m})\right)^T \mathbf{C}_{obs}^{-1} \left(\mathbf{d}_{obs} - g(\mathbf{m})\right) \right] + \left[\left(\mathbf{R_p m}\right)^T \mathbf{C}_{\mathbf{R_p}}^{-1} \left(\mathbf{R_p m}\right) \right], \tag{2}$$

where $\mathbf{m}$ shows the vector of the model parameters, $\mathbf{d}_{obs}$ is the observed data, $g(\mathbf{m})$ represents the forward response of the

90   model, $\mathbf{C}_{\mathbf{obs}}$ consists of the uncertainties of the observed data. The spatial regularization matrix $\mathbf{R}_{\mathbf{p}}$ controls the extent of

variation of each model parameter with respect to its neighbouring cells and $\mathbf{C}_{\mathbf{R}_{\mathbf{p}}}$ denotes the covariance of the spatial

regularization and determines the strength of the regularization term (see Auken and Christiansen, 2004, for details).

The defined misfit function (Eq. (2)) is minimised iteratively. At the nth iteration, the current model $\mathbf{m}_{n}$ is updated as:

$$\mathbf{m_{n+1}} = \mathbf{m_n} + \left(\begin{array}{c} \left[\mathbf{G^T C_{obs}^{-1} G} + \mathbf{R_p^T C_{R_p}^{-1} R_p} + \lambda \mathbf{I} \right]^{-1} \\ \times \left[\mathbf{G^T C_{obs}^{-1}} \left(\mathbf{d_{obs}} - g(\mathbf{m_n}) \right) + \mathbf{R_p^T C_{R_p}^{-1}} \left(-\mathbf{R_p m_n} \right) \right] \end{array} \right), \tag{3}$$

95   where $\mathbf{G}$ is the sensitivity matrix of the data and λ represents the damping factor (see Marquardt, 1963, for details). Two

exit criteria are defined to stop the inversion process. The inversion ends when either the ratio of the values of the misfit

function (Φ) from the updated model and the current one (Φ_{n+1}/Φ_n) is less than 1.0001 or the number of iterations exceeds

35.

Uneven sampling of DC data in terms of wavelength can be problematic in SWT inversion. This can be a serious problem

100   since the inversion might reach the defined stopping criteria without any significant updates in the deeper portion of the

initial velocity model. To address this issue, a wavelength-based weighting scheme was applied in the inversion process to

compensate for the non-uniform sampling of the DC data in terms of wavelength (see Khosro Anjom and Socco, 2019, for

details). Hence, the C_{obs} is modified as:

$$C_{obs} = \begin{pmatrix} \dfrac{\sigma_{1,1}^2}{w_{1,1}} & & 0 \\ & \ddots & \\ 0 & & \dfrac{\sigma_{i,j}^2}{w_{i,j}} \end{pmatrix}, \tag{4}$$

105   where $\sigma_{i,j}$ is the standard deviation of the ith data point of the jth DC, and $w_{i,j}$ is the corresponding weight that is computed

as:

$$w_{i,j} = \frac{\Delta\lambda_{i,j}}{\Delta\lambda_{j,\max}}, \tag{5}$$

where $\Delta\lambda_{i,j}$ represents the wavelength distance between the data point i and its closest data point, and $\Delta\lambda_{j,\max}$ is the

maximum computed wavelength.

3 Results

In this section, we apply straight-ray and curved-ray SWT approaches on four datasets and compare the results. In all the four examples, the DCs are retrieved using an auto-picking code (Papadopoulou, 2021).

3.1 Case study 1: the Blocky model

The Blocky model consists of a sequence of layers with vertically increasing velocity values, surrounding two blocks of velocity anomalies which extend 4 m in horizontal and vertical directions (Figure 1). The receivers are located in a regular grid with 1 m spacing in an area of 20 m × 20 m (Figure 1a). To optimise the shot locations, we defined 441 shots matching the position of the receivers and the aligned receiver couples for each shot were computed. Then, sixteen shots (Figure 1a) were chosen to generate the raw data. They include 11 shots that provided the highest data coverage, and 5 shots at the centre of the model to make sure that enough DCs would cross the two blocks of the velocity anomalies. The synthetic data were generated using a 3D- finite difference code (SOFI3D software described in Bohlen, 2002). The used source is a function of Ricker wavelet with dominant frequency of 40 Hz. To avoid numerical dispersion, the minimum element size is defined in a way to have at least 8 grid-points for the shortest wavelength to model the elastic waves propagation with the interpolation order of 4. To respect the wavelength sampling criteria, a mesh with element size of 0.1 m (in horizontal and vertical dimensions) was defined. To ensure the stability of the simulation, the time stepping was set to 1.0e-5 s to satisfy Courant-Friedrichs-Lewy time stability condition. In total, 971 DCs (Figure 2) were estimated from the raw data using the automatic picking two-station picking code (Papadopoulou, 2021).
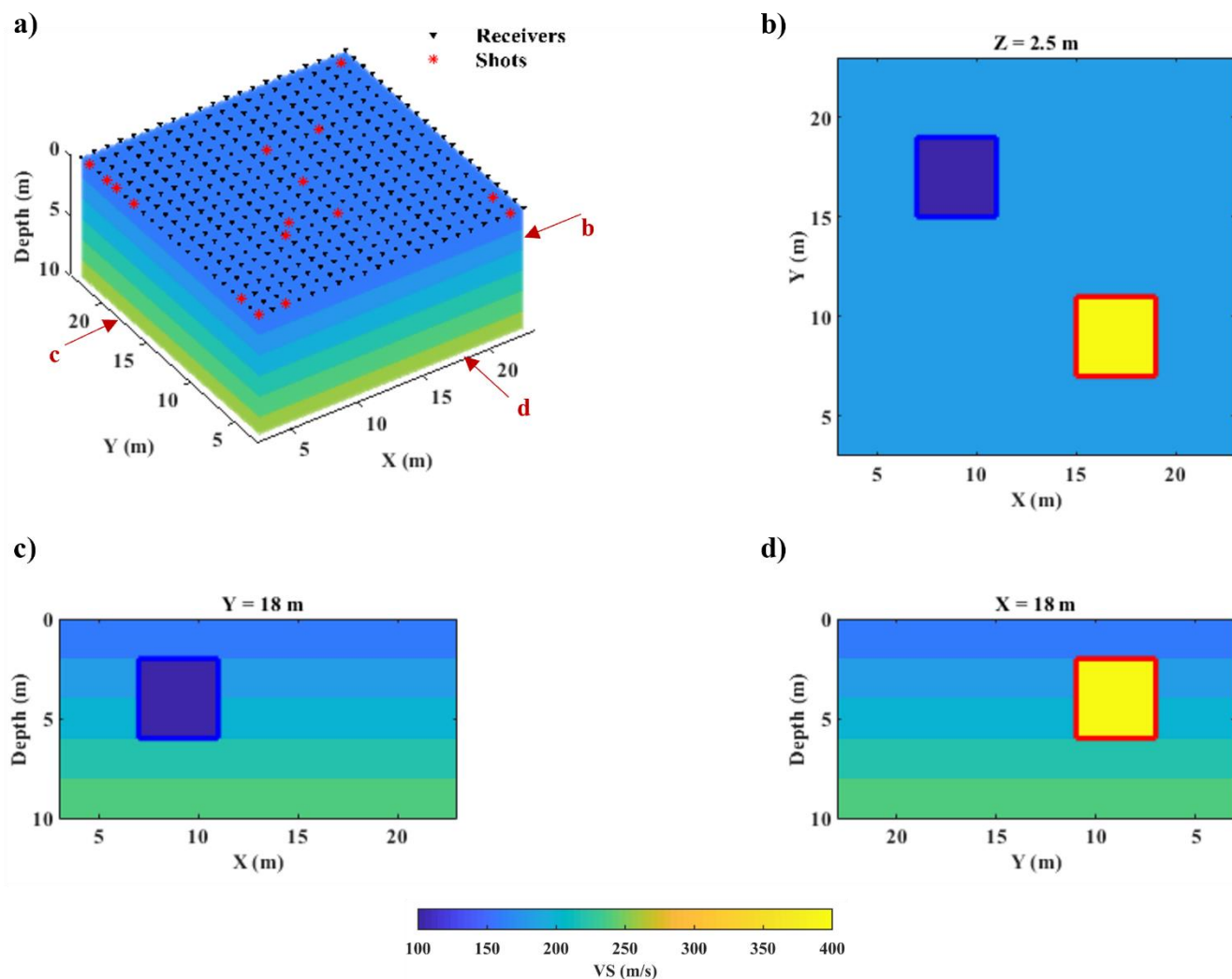
Figure 1. True VS model. **(a)** 3D view of the model together with the acquisition geometry, **(b)** horizontal slice at 2.5 m depth, **(c)** vertical slice at Y=18 m, **(d)** vertical slice at X=18 m. The boundaries of the low- and high-velocity anomalies are superimposed in blue and red, respectively. (X and Y axes do not start from the origin since there is a 3 m absorbing boundary at each side of the model in the simulation)
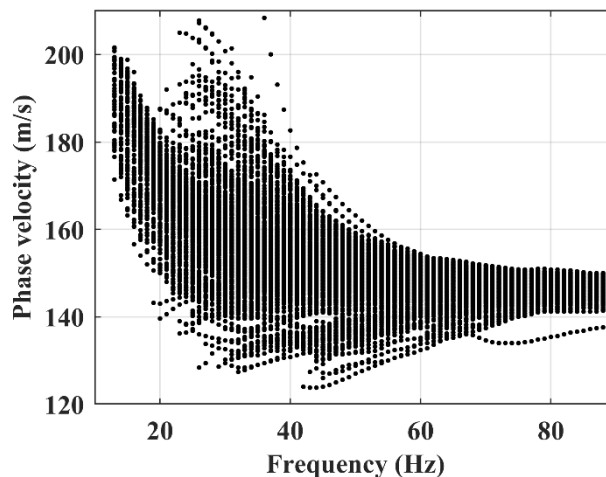
Figure 2. The estimated DCs for the Blocky model.

The initial model for the inversion is defined as a 5-layer 3D model where the thickness of each layer is fixed at 2 m. The horizontal dimensions of each inversion block are 2 m on the side and all blocks have an initial constant VS value of 200 m s^{-1}. The Poisson ratio (v) and ρ values are assumed to the same as the true model and are equal to 0.33 and 2000 kg m^{-3} in the whole subsurface. The same initial model is used as the starting model for the SWT inversion in both straight- and curved-ray methods. The inversion ends when the stopping criteria are satisfied. The VS models at the last iteration of the inversion are displayed in Figure 3.
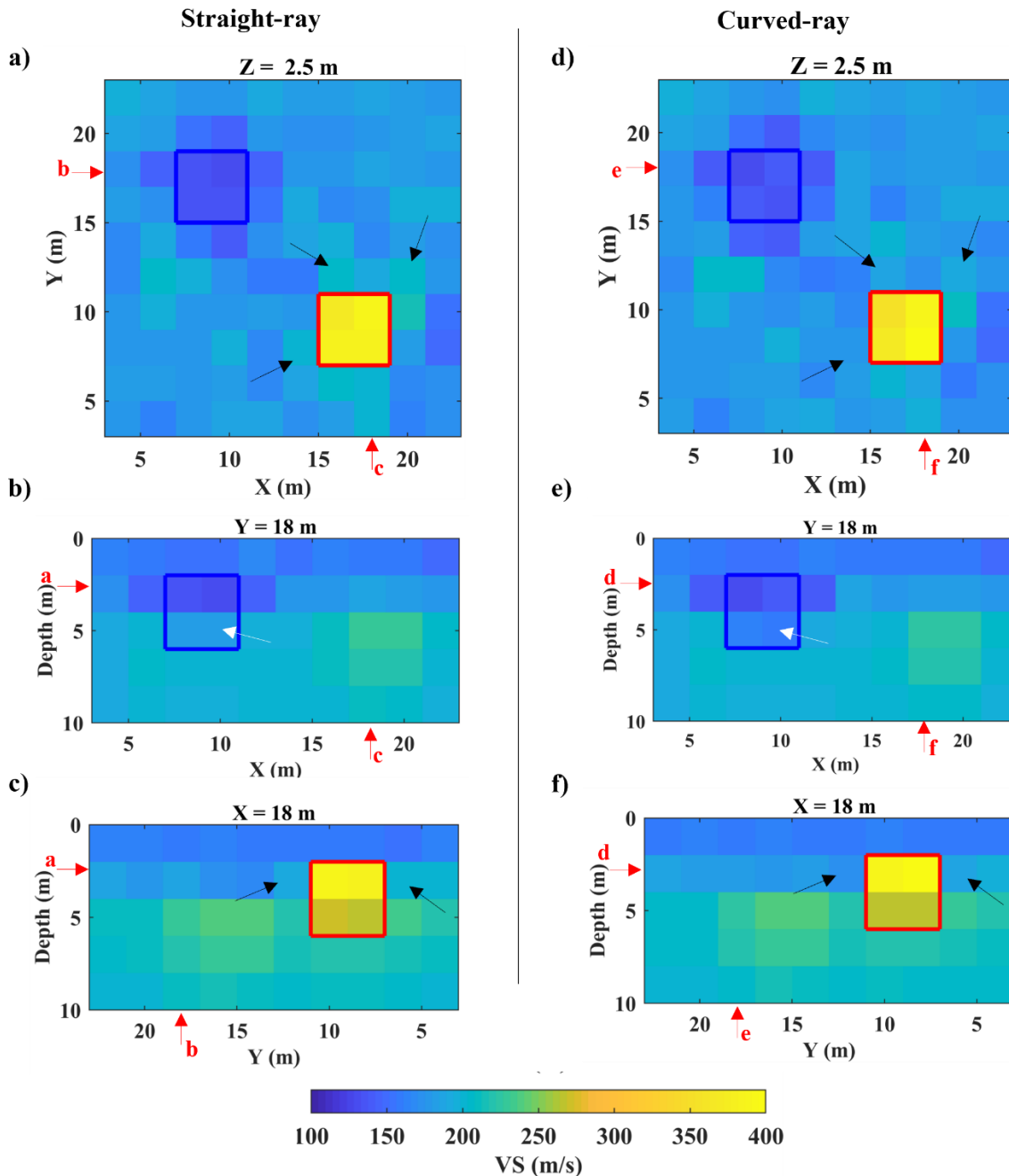
Figure 3. The VS models from SWT inversion. Straight-ray SWT results are shown at: **(a)** 2.5 m depth, **(b)** Y=18 m, **(c)** X=18 m, and the results of the curved-ray for the same slices are displayed at subfigures **(d)** to **(f)**. The boundaries of the low- and high velocity blocks are superimposed in blue and red. Each red arrow shows the location of the corresponding subfigure in the current cross-section. The black and white arrows mark the blocks in which the curved-ray approach provides better results.

Figure 3 shows that straight- and curved-ray SWT have modelled the location and the value of the high-velocity anomaly quite accurately. The model from the curved-ray method is slightly superior at the grid blocks surrounding the high-velocity

150   box (the black arrows in Figure 3). In case of low-velocity anomaly, curved-ray SWT has provided better results, since the

bottom half of the low velocity block is better resolved by the curved-ray approach (the white arrows in Figure 3b and e).

3.2 Case study 2: the Sand Bar model

The Sand Bar model is designed to simulate a saturated environment where a sand layer is buried in unconsolidated clays.

The model contains a curved-shape high-velocity anomaly (the sand layer) embedded between two low-velocity clay layers

(Figure 4). The parameters of the true model are shown in Table 1. The receivers are distributed at the surface as a regular

155   grid with 2 m spacing (Figure 4a). We defined sources at the same location of receivers and for each source, we computed

the aligned receiver pairs. Then, we picked 13 shots (Figure 4a) which provided the highest data coverage to generate the

synthetic data. The same finite difference code used for the Blocky model was used to obtain the Sand Bar synthetic dataset.

The source is a function of Ricker wavelet with dominant frequency of 40 Hz, and the minimum element size of the mesh

grid was set to 0.1 m to prevent numerical dispersion. The time stepping was equal to 1.0e-5 to avoid simulation instability.

160   A total number of 1207 dispersion curves (Figure 5) were retrieved from the raw data.

Table 1. Geophysical parameters of the true model.

Material	VS (m s^{-1})	VP (m s^{-1})	Computed v	h (m)	ρ (kg m^{-3})
Clay- 1st layer	80	1700	0.497	3-6	1750
Sand	150	2000	0.499	3	1900
Clay- last layer	100	1850	0.498	4	1950
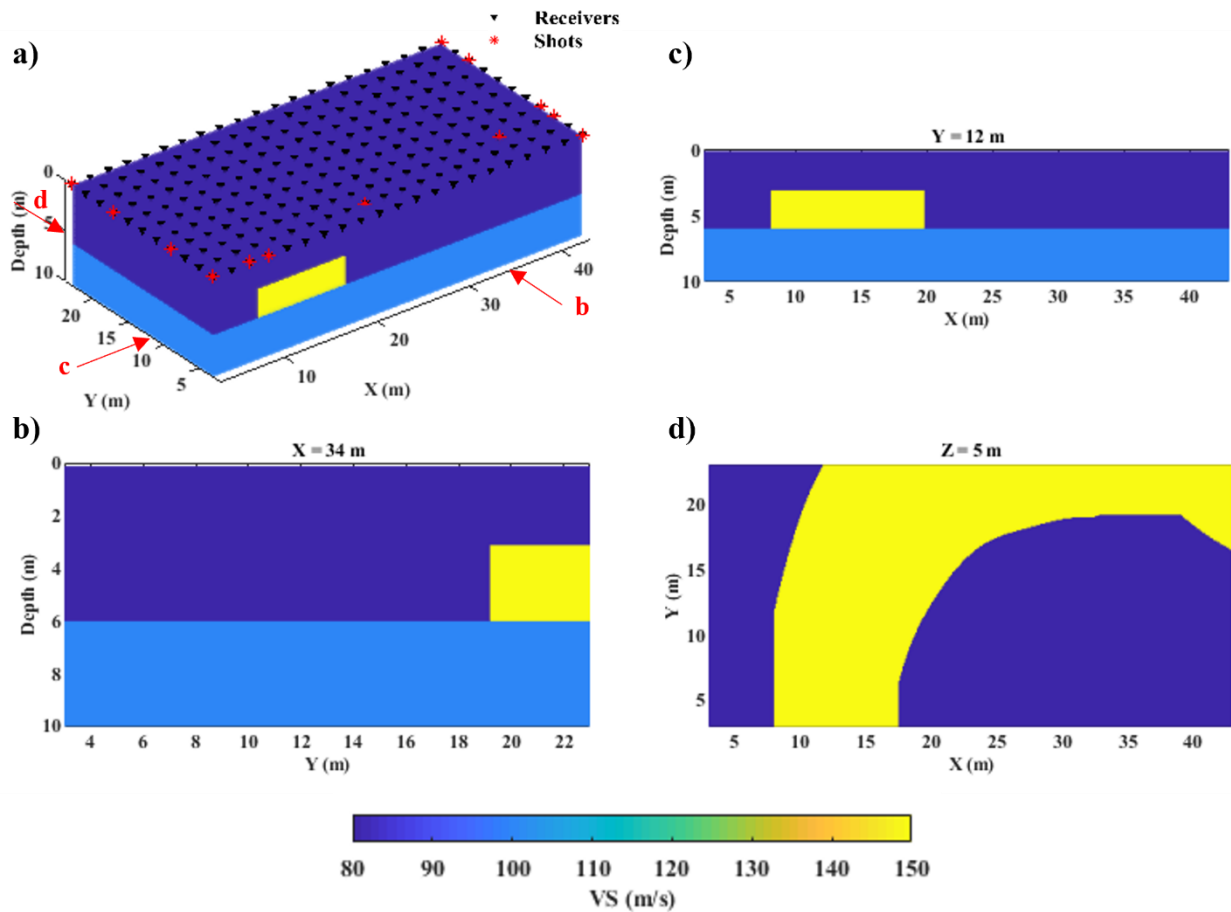
Figure 4. True VS model. **(a)** 3D view of the Sand Bar model together with the acquisition geometry. The arrows show the location of the cross-section in the corresponding subfigure. **(b)** Vertical slice at X=34 m, **(c)** vertical slice at Y=12 m, **(d)** horizontal slice at 5 m depth.
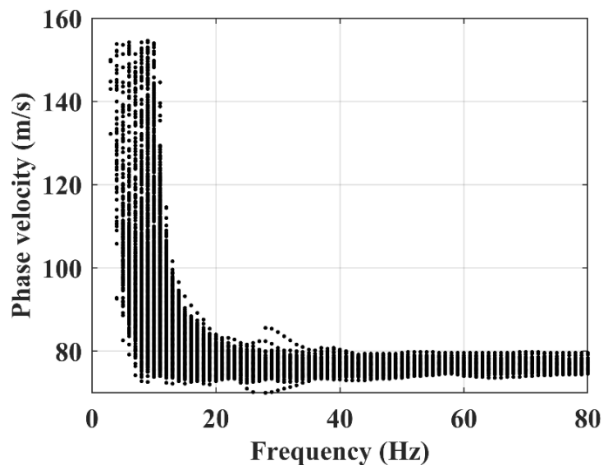
Figure 5. The extracted DCs for the Sand Bar model.

The defined initial model is a 3D model with 10 layers of constant 1 m thickness where the VS values are fixed at 80 m s⁻¹. The inversion blocks are 2 m in horizontal dimensions. The initial Poisson ratio and density values are set equal to the values of the true model (Table 1). The SWT inversion results for one horizontal and two vertical slices of the model are shown in

170   Figure 6.
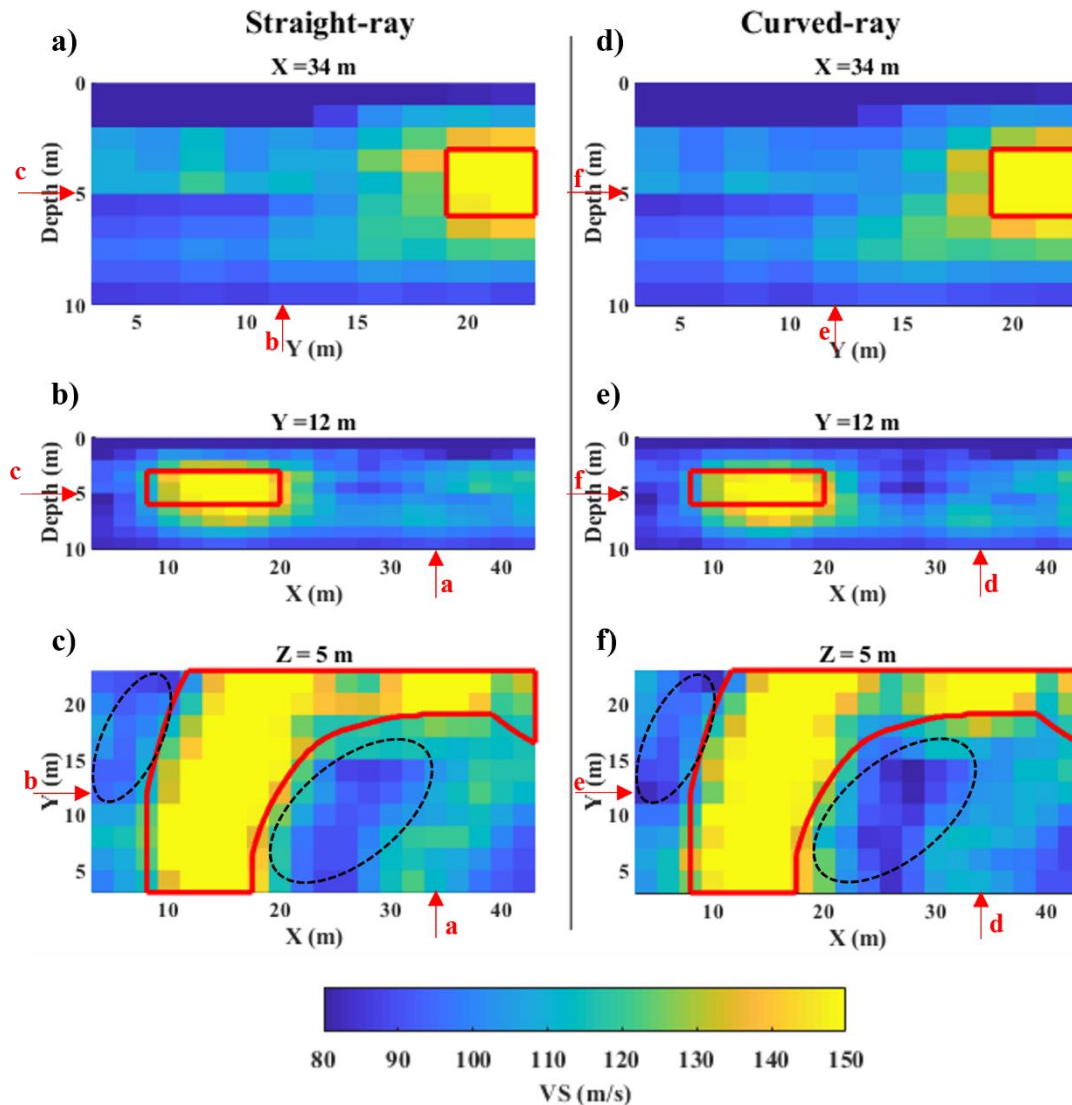
Figure 6. SWT inversion results. Straight-ray SWT results are shown at: **(a)** X=34 m, **(b)** Y=12 m, **(c)** Z=5 m, and the results of the curved-ray for the same slices are displayed at subfigures **(d)** to **(f)**. The boundaries of the sand layer are superimposed in red. Each red arrow shows the location of the corresponding subfigure in the current cross-section.

175   We can see in Figure 6 that the VS models from both approaches are like each other. Figure 6 shows that both methods have

successfully located the high-velocity anomaly. Not only the velocity values are close to the true model (Figure 4b to d), also

the shape of the anomaly has been retrieved clearly. The vertical slices at X (Figure 6a and d) and Y directions (Figure 6b

and e) do not display significant differences. However, the areas marked in dashed black in the horizontal slices (Figure 6c and f) shows that the boundaries of the anomaly are clearer in the curved-ray approach (Figure 6f) and also the VS values in
180 these areas are closer to the true VS value (Figure 4d).

3.3 Case study 3: Pijnacker field

The data were acquired in a field near Pijnacker, South Holland, Netherlands (Figure 7a). An area of 27 m×30 m was investigated by 120 geophones and 59 shot locations (Figure 7b). The shot locations were optimised for the locations inside the array area. A total number of 868 shots were defined as regular grids of 1m spacing and 15 shot locations which provided
185 the highest coverage were chosen as the optimised shot positions. Moreover, 44 shot locations were chosen outside the acquisition area, each one at 3 m distance from every geophone located at the outer boundary of the acquisition area. The source was a vibrator that emitted a linear sweep signal from 2 to 100 Hz for 5 seconds at a force level of 1150 N. Some of the available shallow well data close to the field are depicted in Figure 7c. They show that the field mainly consists of clay, together with peat and possibly sand in some locations. Using the automatic picking code (Papadopoulou, 2021), 972 DCs
190 (Figure 7d) were extracted from the data.

a)

b)

c)

d)
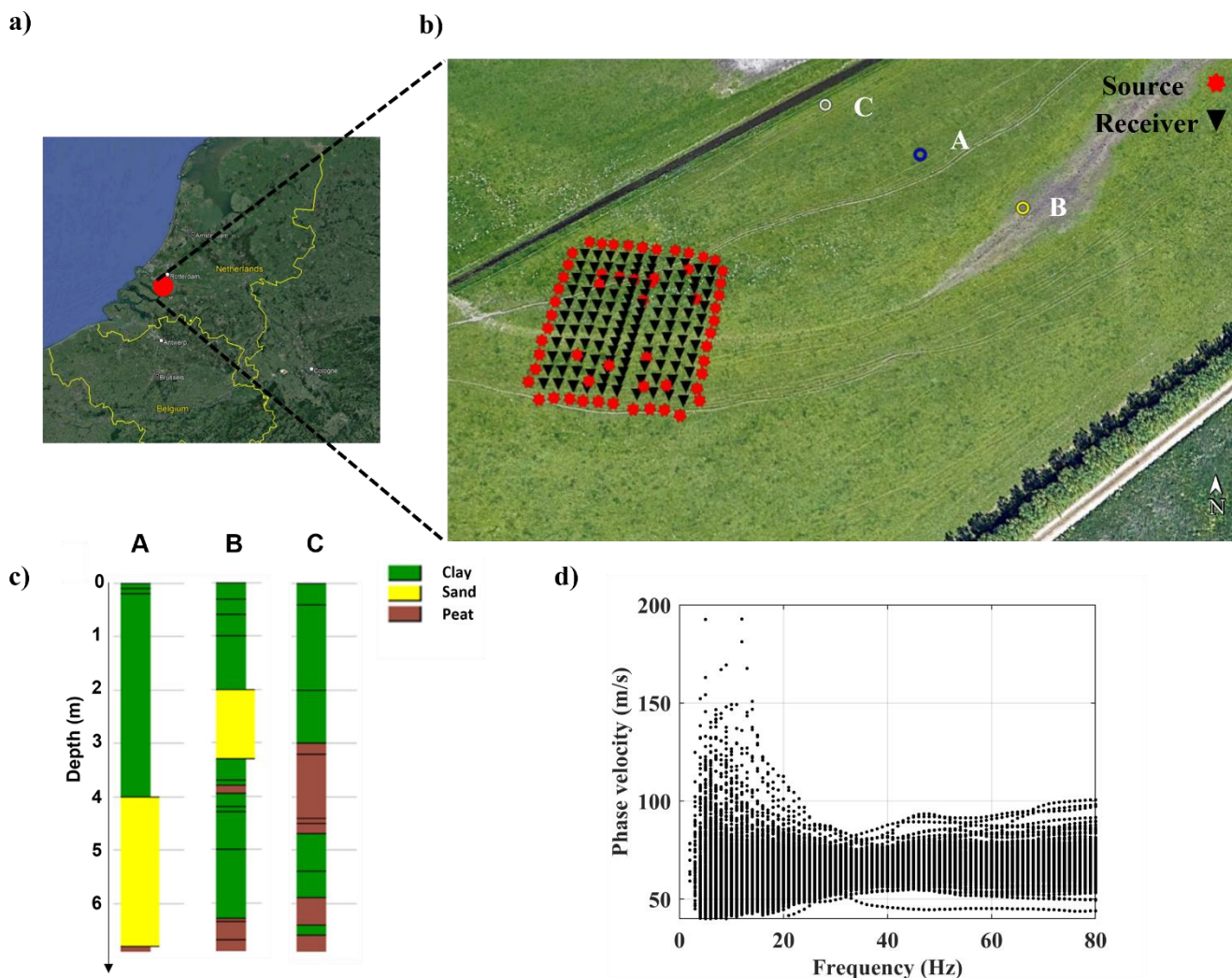
Figure 7. (a) Aerial view of Netherlands with the red circle marking the location of the Pijancker field (© Google Earth). **(b)** The acquisition geometry (© Google Earth), **(c)** the available well data near the field. The location of each well is shown with the corresponding letter in subfigure (b). **(d)** The retrieved DCs.

Each inversion block extends 3 m horizontally. In this case, the initial model contains 6 layers where the layers get thicker with depth. The first two layers are 1 m thick, following by two layers of 2 m and two of 3 m. The initial model is defined regardless of the well information. The well data are used later to assess the inversion results. The inversion started from an initial VS value of 60 m s^{-1}. The values of the initial model parameters are reported in Table 2. The SWT inversion results for straight- and curved-ray methods are depicted in Figure 8.

Table 2. Parameters of the initial model for the inversion.

Layer	1	2	3	4	5	6
VS (m s^{-1})	60	60	60	60	60	60
v	0.45	0.45	0.45	0.45	0.45	0.45
h (m)	1	1	2	2	3	3
ρ (kg m^{-3})	1700	1700	1700	1700	1700	1700
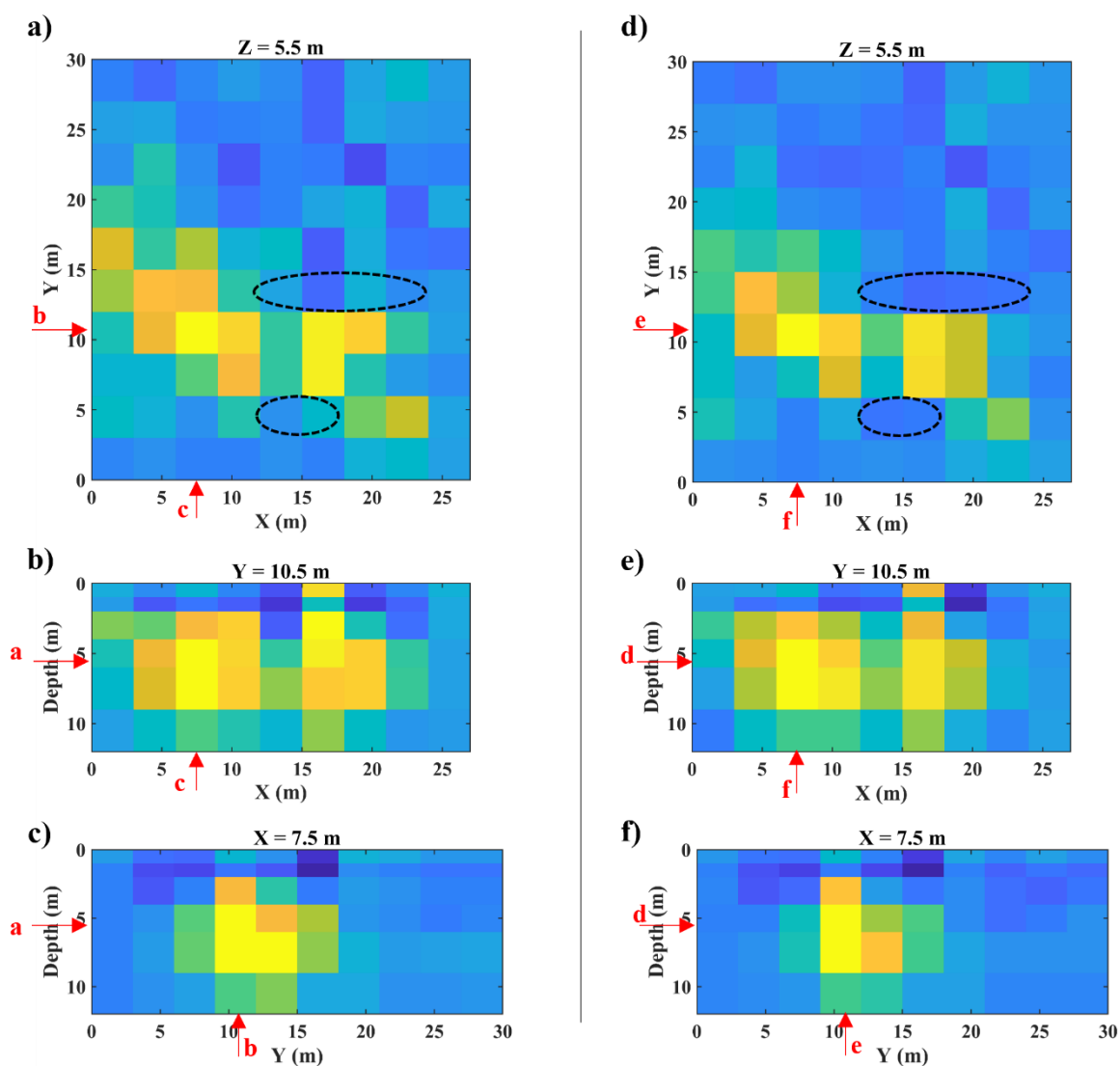
Figure 8. SWT inversion results. Straight-ray SWT results are shown at: **(a)** 5.5 m depth, **(b)** Y=10.5 m, **(c)** X=7.5 m, and the results of the curved-ray for the same slices are displayed at subfigures **(d)** to **(f)**. Each red arrow shows the location of the corresponding subfigure in the current cross-section. The dashed black marks the blocks in which the VS from the straight- and curved-ray are considerably different.

We can see in Figure 8 that also in this case the VS models from the straight- and curved-ray SWT are similar. The difference between the horizontal slices (Figure 8a and d) are clearer than the vertical ones. As shown in dashed black, we can see that the cells around the high velocity portion have lower VS values in the curved-ray (Figure 8d) than straight-ray (Figure 8a). A previous 2D full waveform study (Bharadwaj et al., 2015) on a clay-field which was not very far from the field location of our study, obtained a VS model in range of 40-80 m s^{-1} up to 15 m depth. This is in agreement with the inversion results shown in Figure 8. The high velocity portions relate to the sand. It can be seen in the vertical slices in Figure 8 that the depth of high-velocity part (sand layer) is mainly in range of 2-9 m which seems reasonable given the a priori well data (Figure 7c).

3.4 Case study 4: CNR field

The field data were acquired at National Research Council (CNR) headquarter in Turin, Italy (Figure 9a and b). The site consists of compacted sand and gravel formations surrounding an artificial loose sand body. The sand body occupies an area of 5 m × 5 m at the surface and the maximum depth reaches 2.5 m. The receiver layout consists of 4 lines which are 2.5 m apart. Each acquisition line includes 18 vertical 4.5 Hz geophones with 0.5 m spacing. The used source was an 8 kg hammer. The acquisition was carried out in 83 shot locations. Figure 9c shows the acquisition setup. The data were processed using the auto-picking code and the low quality DCs were rejected in a data-driven approach (for details, see Papadopoulou, 2021), and in total, 315 DCs (Figure 9d) were estimated from the data.

a)

b)

c)

d)
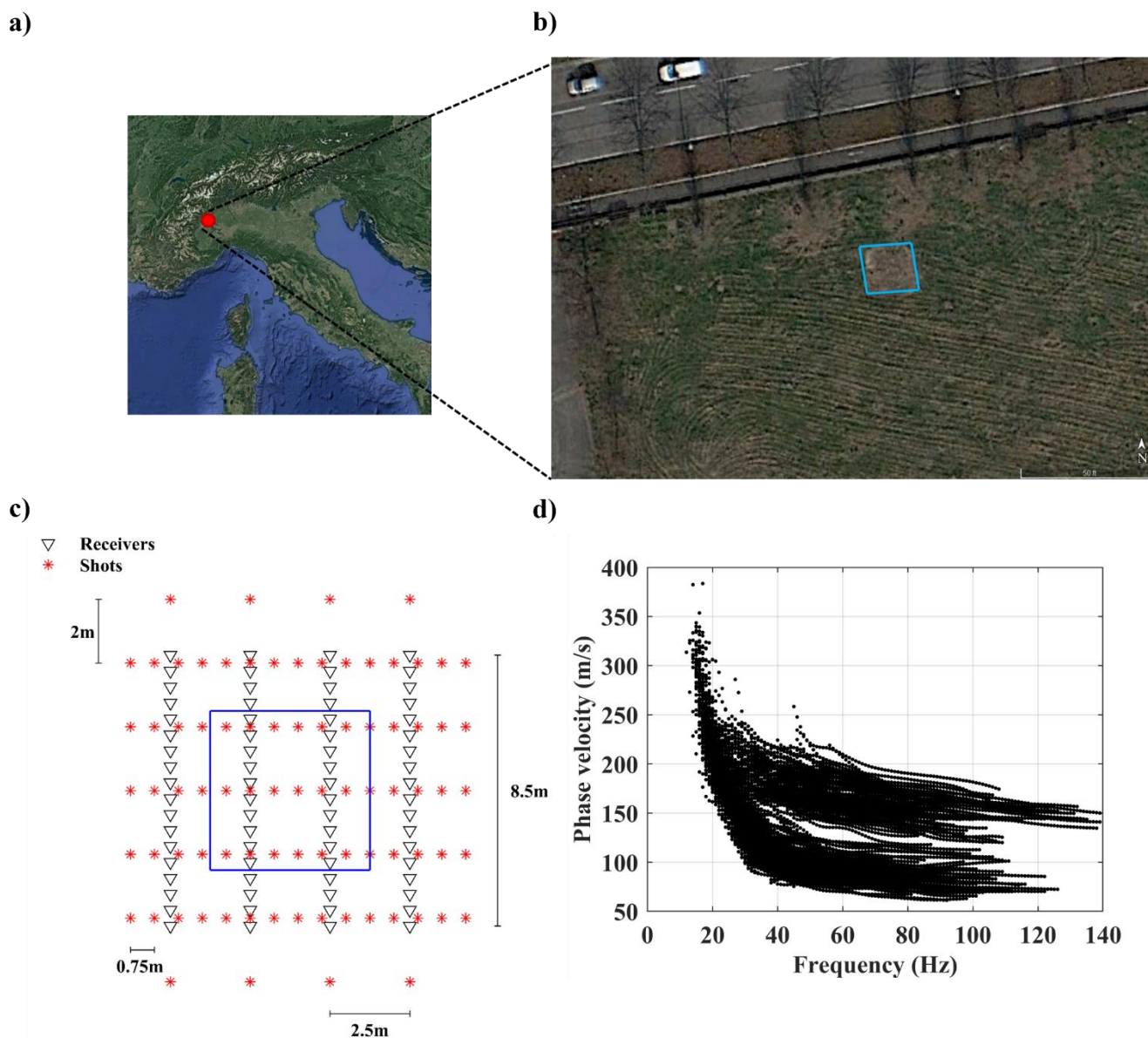
Figure 9. **(a)** Aerial view of Italy with the red circle shows the location of the site (© Google Earth). **(b)** A closer view of the CNR site (© Google Earth). **(c)** The acquisition outline. The boundaries of the sand body are highlighted in blue. **(d)** The estimated DCs.

225   The inversion started from an 8-layer 3D model where the horizontal and vertical sizes of each grid is 0.5 m, and VS is equal to 200 m s^{-1}, ν is equal to 0.33, and density is fixed at 2000 kg m^{-3}. Both straight- and curved-ray SWT inversion started from the same initial model and the results are presented in Figure 10.
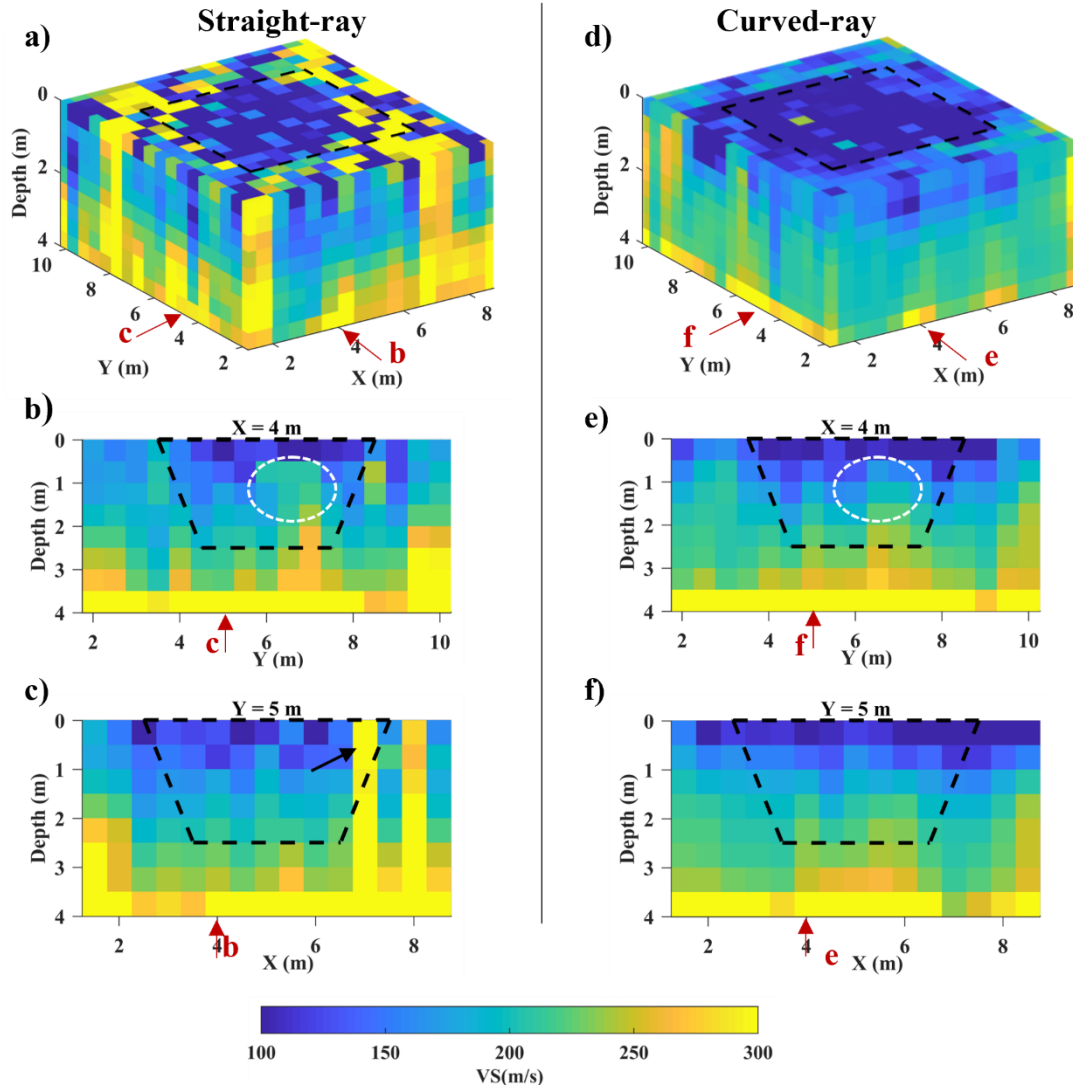
Figure 10. The VS models from SWT inversion. The boundaries of the sand body are superimposed in dashed black. The red arrows
230   correspond to the location of the vertical slices. The results of the straight-ray are shown as: **(a)** the 3D view of the VS model, **(b)** the
vertical slice at X=4 m, **(c)** at Y=5 m, and the corresponding results from the curved-ray SWT inversion are displayed in subfigures **(d)** to
(f).

Figure 10 shows that the difference between straight- and curved-ray models are more pronounced in this example. There are

some cells with relatively high velocity values inside the sand body in the model obtained from the straight-ray (Figure 10a).

235   The boundaries of the loose sand body at the surface are better retrieved by the curved-ray SWT (Fig. 10d). The area shown

in dashed white in Figure 10b and e shows that the gradual increase of the VS values with depth inside the sand body is

clearer in the model from the curved-ray (Figure 10e). The black arrow in Figure 10c shows the high velocity cells inside the

loose sand body in the retrieved model from the straight-ray SWT. This artefact does not exist in the corresponding slice

from the curved-ray SWT (Figure 10f).

4 Discussion

We have applied straight-ray and curved-ray SWT on four datasets and compared the results. In this section, we investigate the results in more details considering ray paths, data weighting, models and data misfits, and computational cost.

4.1 Ray paths

The improvement of the model obtained by the curved-ray SWT with respect to straitgh-ray SWT, particularly at the boundaries of velocity anomalies has been shown in the synthetic and real world examples. Some selected examples of the computed ray paths at the last iteration of the curved-ray SWT are depicted in Figure 11.
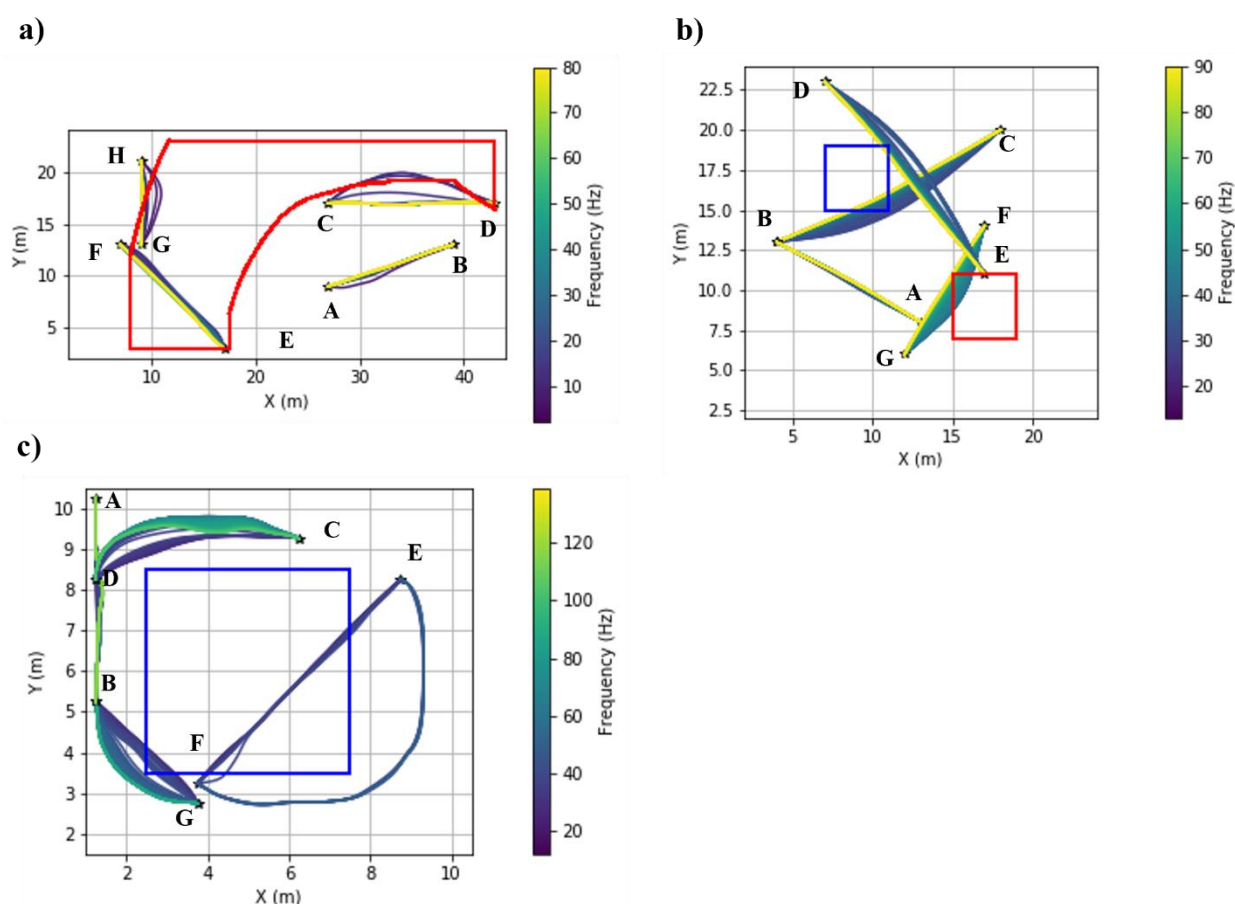
Figure 11. Examples of the computed ray paths at the last iteration of the curved-ray SWT inversion for: **(a)** the Sand Bar model, **(b)** the Blocky model, **(c)** the CNR field. The boundaries of the low- and high-velocity anomalies are shown in blue and red, respectively. The receiver locations are labelled as A-H.

In all the three models in Figure 11 the receivers A and B are located outside the velocity anomalies, and we see that the computed ray paths between them do not cross the anomalies. Therefore, the obtained paths do not deviate considerably from straight lines. In Figure 11a, the high-velocity anomaly exists at the depth range of 3-6 m. Hence, we can see that the

high-frequency components of the DCs, which correspond to the shallow parts of the model, do not deviate from straight
255   lines. But the lower frequencies (i.e., higher wavelengths) for the C-D and G-H pairs have deviated from straight lines and
travelled through the high-velocity parts. In Figure 11b, the depth of velocity anomalies is in range of 2 to 6 m. We see that
also in this case the ray paths for higher frequencies have almost no deviations from straight lines since they do not cross the
anomalies. However, we can see for the obtained paths between B-C and D-E pairs that the lower frequencies have bypassed
the low-velocity anomaly. Similarly, lower-frequencies in case of the G-F pair have deviated from straight paths and
260   travelled through the high-velocity anomaly. In Figure 11c, the sand body (low-velocity anomaly) starts at the surface and
reaches to maximum of 2.5 m depth. Its area shrinks from 5 m × 5 m at the surface to 3 m × 3 m at 2.5 m depth. The
shrinkage in size of the anomaly can be seen in the computed path for the B-G, C-D, and E-F pairs, where the degree of the
deviation from the straight line decreases as the depth increases (frequency decreases).

Even though the exact boundaries of the anomaly (sand layer) are unknown for the Pijnacker field, the computed ray paths
265   can provide helpful insights. For instance, the computed ray paths from straight- and curved-ray SWT, for the DCs data with
the wavelengths in range of 6-9 m are displayed in Figure 12.
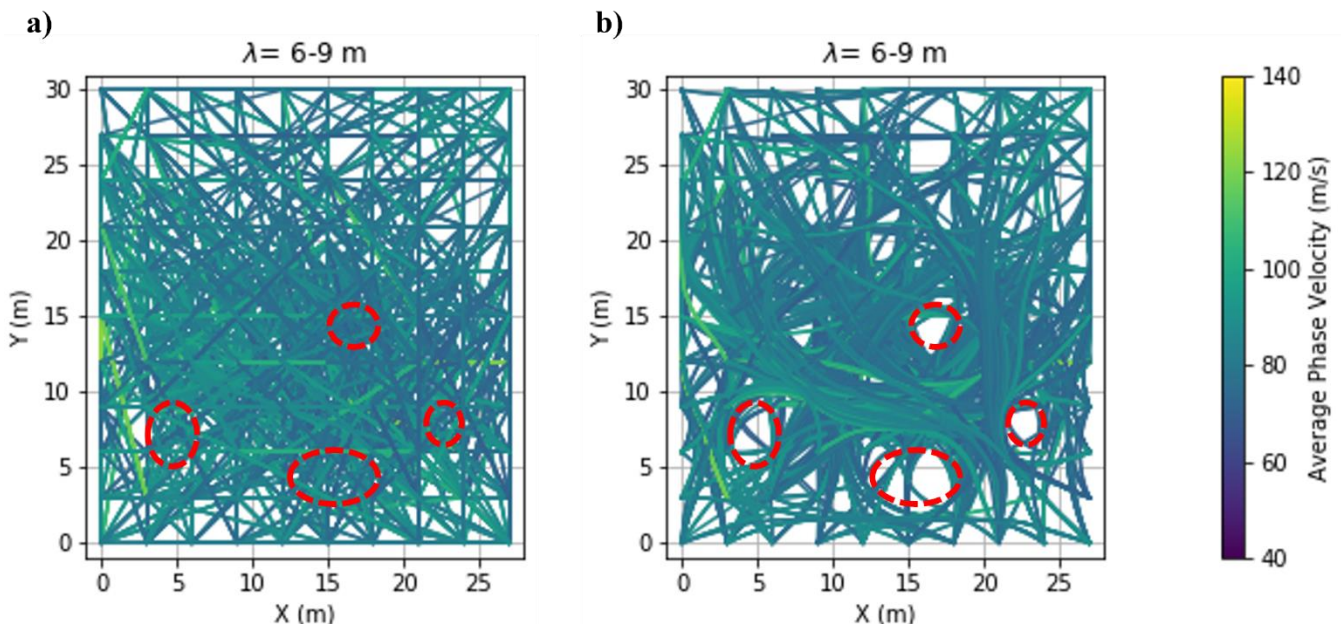
Figure 12. The computed ray paths for the data points with wavelengths in range of 6-9 m from: **(a)** the last iteration of the straight-ray,
(b) the last iteration of curved-ray SWT inversion. The colours of ray paths correspond to the computed path-averaged phase velocity
270   along the path.

Since the initial VS model is vertically and horizontally homogeneous, the initial ray paths for both straight- and curved-ray
SWT are straight lines. As shown in Figure 12a, the ray paths do not change during the inversion in the straight-ray
approach. However, the paths are updated at every iteration of the curved-ray SWT inversion. We see that some areas in
Figure 12b (shown in dashed red) are bypassed by almost all the rays even though the data coverage of these areas in the
275   straight-ray approach (Figure 12a) is considerably high. Therefore, these portions correspond to the low velocity materials,

i.e., clay and peat. The area between these low-velocity portions has both higher concentration of ray paths and higher average phase velocity values. Therefore, they probably show the sand layer. These locations agree with the obtained VS model from the curved-ray SWT inversion (Figure 8d).

4.2 Misfits and computational costs

280   We have shown the inversion results from the straight-ray and curved-ray SWT. In this part, we compare the results quantitatively. We carried out the inversions on 40 cores on a cluster with the processor type of Intel® Xeon® E5-2650 v3. In For each parameter, the values from the straight-ray and curved-ray approaches are averaged and the corresponding relative difference is shown in the last column of Table 3.

Table 3, we report the number of iterations (n_i), the running time (r_t), the maximum memory consumption during the

285   inversion process (mem_{max}), the relative data misfit at the last iteration of the inversion (e_d), the relative model misfit for all cells (e_m) and only the ones in the depth range of the target (e_t), and the cost of inversion to be run at Microsoft cloud service. We define the relative data misfit (e_d) as:

$$e_d = mean\left(\frac{\left|\mathbf{d}_{obs} - \mathbf{fw}\left(\mathbf{m}_{final}\right)\right|}{\mathbf{d}_{obs}}\right), \tag{6}$$

where $\mathbf{d}_{obs}$ is the vector of the experimental DCs and $\mathbf{fw}\left(\mathbf{m}_{final}\right)$ represents the computed forward response of the model at the final iteration of the inversion. In case of the synthetic examples (the Blocky and Sand Bar models), we can compare the

290   obtained VS models from the inversion (VS_{final}) with the true model (VS_{true}). We compute the average relative model misfit (e_m) as:

$$e_m = mean\left(\frac{\left|\mathbf{VS}_{true} - \mathbf{VS}_{final}\right|}{\mathbf{VS}_{true}}\right), \tag{7}$$

For each parameter, the values from the straight-ray and curved-ray approaches are averaged and the corresponding relative difference is shown in the last column of Table 3.

Table 3. The quantitative comparison of straight- and curved-ray SWT.

SR \ CR	Sand Bar	Blocky	CNR	Pijnacker	CR-SR
n_i	35 / 19	16 / 20	31 / 15	23 / 10	-39 %
r_t (h)	15.17 / 18.99	3.13 / 6.1	1.97 / 1.70	8.31 / 7.74	+23 %
mem_{max} (GB)	17.25 / 18.41	2.85 / 3.85	3.89 / 3.94	40.35 / 40.41	+11 %
e_d (%)	1.119 / 1.121	0.985 / 0.987	4.40 / 7.21	9.25 / 9.81	+21 %
e_m (%)	15.80 / 15.11	8.71 / 8.48	-	-	-4 %
e_t (%)	23.19 / 20.36	9.74 / 9.23	-	-	-11 %
$Cost$ ($\$$)	64.3 / 80.5	13.3 / 25.9	8.4 / 7.2	35.2 / 32.8	+23 %

295

We can see in For each parameter, the values from the straight-ray and curved-ray approaches are averaged and the corresponding relative difference is shown in the last column of Table 3.

Table 3 that in all examples except for the Blocky model, curved-ray SWT has converged in less iterations than the straight-ray. However, the curved-ray SWT has increased r_t by 23 % compared to straight-ray. For all the case studies, curved-ray

300   SWT needed more memory (11 % by average) than straight-ray. In terms of data misfit (e_d), straight-ray approach has provided better performance than the curved ray. We can also see that the difference between the obtained e_d values from the straight- and curved-ray SWT is negligible in case of the synthetic examples (the Sand bar and Blocky models), but the difference is more pronounced for the field examples (the CNR and Pijnacker). Despite having higher e_d, the curved-ray approach has produced lower model misfits than straight-ray. Using curved-ray SWT has decreased the overall model misfit

305   (e_m) and the target model misfit (e_t) by 4 % and 11 %, respectively. Finally, we see in For each parameter, the values from the straight-ray and curved-ray approaches are averaged and the corresponding relative difference is shown in the last column of Table 3.

Table 3 that using curved-ray SWT has increases the computational cost by an average of 23 %.

4.3 Impact of the data coverage

310   In all the presented examples, the computed VS models from the straight-ray and curved-ray SWT do not differ significantly except for the CNR field. The reason for this difference can be the low data coverage, particularly in the shallower portion of the medium. Figure 14 depicts the ray paths of the DCs data with the wavelengths in range of 0-1 m.
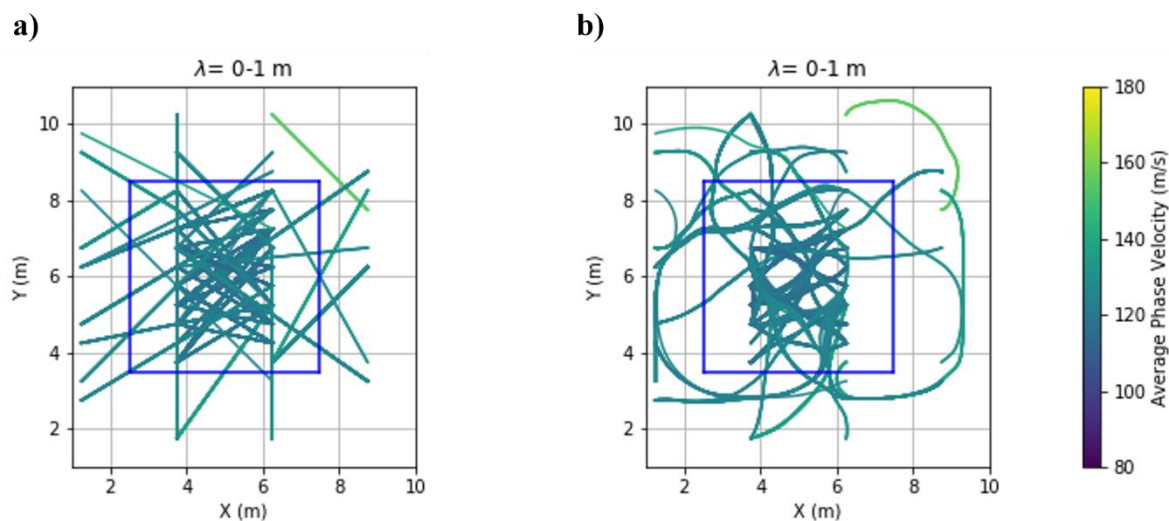
Figure 13. The ray paths for the data points with wavelengths in range of 0-1 m from: **(a)** the last iteration of the straight-ray, **(b)** the last iteration of curved-ray SWT inversion. The boundaries of the sand body at the surface are superimposed in blue. The colours of ray paths correspond to the computed path-averaged phase velocity along the path.

We can see in Figure 13a that some areas of the medium are not covered with straight-rays, especially outside the sand body. It should be noted that for both cases, the ray paths at the first iteration are straight lines since the initial model has a constant VS value for all cells. However, in the curved-ray approach (Figure 13b) the ray paths are flexible and can adjust to the updated subsurface velocity during the inversion process. Figure 13b also shows that the ray paths have been responded properly to the edges of the loose sand body, travelling through the faster part of the model.

4.4 Weighting effect

As mentioned previously, uneven sampling of DC data in terms of wavelength can be problematic in SWT inversion. For instance, most of the extracted DC data (81 %) of the Pijnacker field have wavelengths less than 3 m while the available well data from the area suggest that the depth of the target is expected to vary in range of 2-7 m. This can be a serious problem since the inversion might reach the defined stopping criteria without any significant updates in the deeper portion of the initial velocity model. Figure 14 shows the obtained VS models with (Figure 14a and b) and without (Figure 14c and d) the wavelength-based weighting at 5.5 m depth.
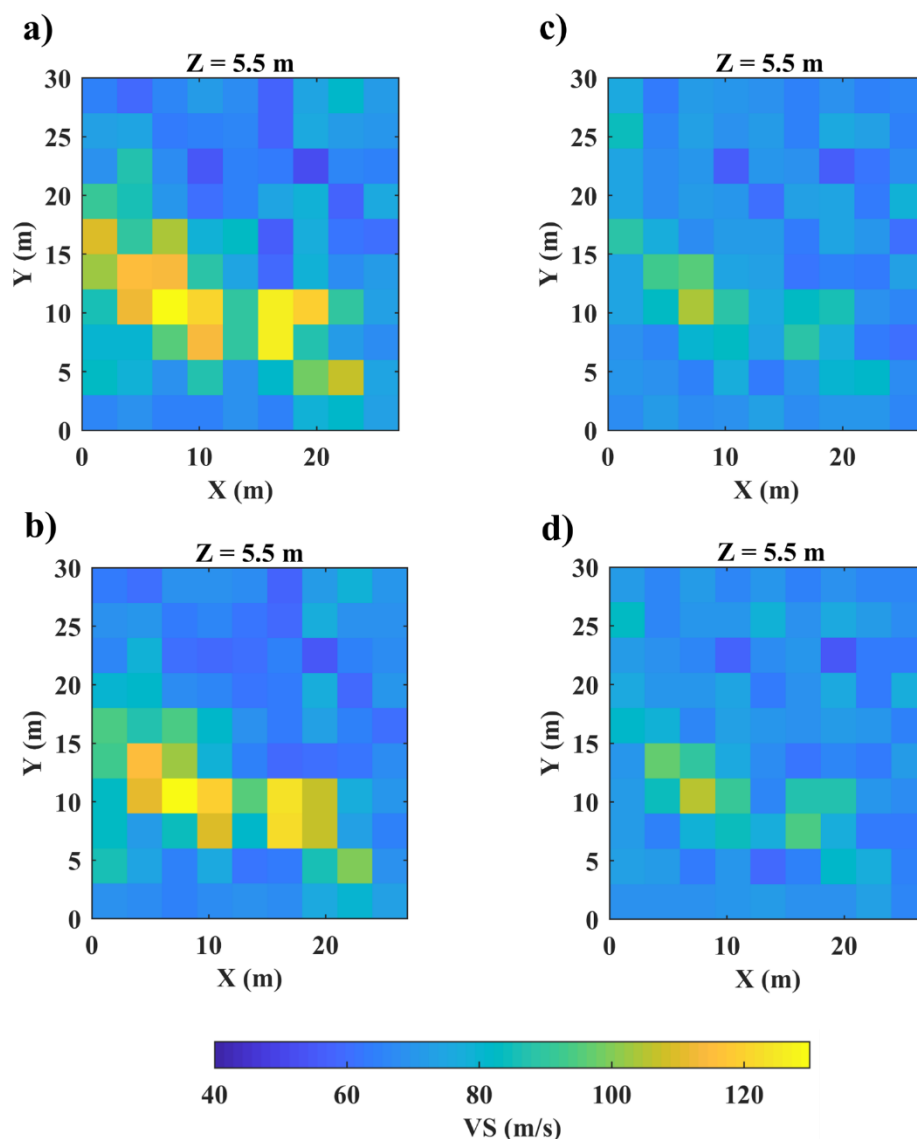
Figure 14. The impact of weighting on the SWT inversion results. The computed VS model at the depth of 5.5 m from: **(a)** weighted straight-ray, **(b)** weighted curved-ray, **(c)** non-weighted straight-ray, **(d)** non-weighted curved-ray SWT.

In Figure 14, we can see the improvement of the model after applying the wavelength-based weighting method (Figure 14a and b) compared with the non-weighted model (Figure 14c and d) where the non-weighted inversions have barely retrieved any pattern to model the target (sand layer).

5 Conclusions

We have applied straight-ray and curved-ray SWT to four datasets. We have shown that in all the examples, SWT is a powerful tool to estimate the shallow subsurface VS distribution in 3D. The obtained results from the curved-ray SWT are better than results from the straight-ray method, particularly at modelling the edges of the anomalies. By comparing the obtained results from the synthetic and field examples we can say that in case of high data coverage, the straight-ray SWT can provide 3D VS models which are very close to curved-ray approach but with lower computational cost. However, if the data coverage is not high enough, curved-ray SWT provides significant model improvement. We also recommend analysing the data coverage to choose the proper weighting method.

Code and data availability. The data may be available by contacting the corresponding author. The code may also be available by contacting the corresponding author after carrying out some additional work to make it user-friendly.

Author contributions. MK worked on the processing and inversion of all the datasets, with coordination and supervision of ES and LVS. MK and ES contributed to seismic data acquisition in Pijancker field and LVS coordinated the seismic data acquisition in the CNR site. MK wrote the original paper draft, with contribution from all the authors.

Competing interests. The contact author declares that neither him nor his co-authors have any competing interests.

Acknowledgements

We would like to thank Seismic Mechatronics for providing the vibrator source, CNR group for giving access to data acquisition, Compagnia di San Paolo for funding the PhD of Mohammadkarim Karimpour, and all the people involved in data acquisition.

References

Auken, E. and Christiansen, A.V.: Layered and laterally constrained 2D inversion of resistivity data, Geophysics, 69, 752–761, https://doi.org/10.1190/1.1759461, 2004.

Barone, I., Kästle, E., Strobbia, C., and Cassiani, G.: Surface wave tomography using 3D active-source seismic data, Geophysics, 86, EN13-EN26, doi: 1 0.1190/GEO2020-0068.1, 2021.

Bohlen, T.: Parallel 3-D viscoelastic finite-difference seismic modelling, Comput. Geodci., 28, 887-899, https://doi.org/10.1016/S0098-3004(02)00006-7, 2002.

Boiero, D.: Surface wave analysis for building shear wave velocity models: Ph.D. thesis, Politecnico di Torino, 2009.

Boschi, L. and Dziewonski, A. M.: High- and low-resolution images of the Earth's mantle: Implications of different approaches to tomographic modelling, J. Geophys. Res, 104, 25,567–25,594, https://doi.org/10.1029/1999JB900166, 1999.

Bharadwaj, P., Mulder, W. A., Drijkoningen, G. G., and Reijnen, R.: Looking Ahead of a Tunnel Boring Machine with 2-D SH Full Waveform Inversion, 77th EAGE Conference and Exhibition, https://doi.org/10.3997/2214-4609.201412803, 2015.

Boschi, L. and Ekström, G.: New images of the Earth's upper mantle from measurements of surface wave phase velocity
370 anomalies, J. Geophys. Res.: Solid Earth, 107, 1-14, https://doi.org/10.1029/2000JB000059, 2002.

Bozdag, E. and Trampert, J.: On crustal corrections in surface wave tomography, Geophys. J. Int., 172, 1066-1082, https://doi.org/10.1111/j.1365-246X.2007.03690.x, 2008.

Bussat, S. and Kugler, S.: Offshore ambient-noise surface-wave tomography above 0.1 Hz and its applications, The Leading Edge, 30, 514-524, https://doi.org/10.1190/1.3589107, 2011.

375 Da Col, F., Papadopoulou, M., Koivisto, E., Sito, L., Savolainen, M., and Socco, L. V.: Application of surface-wave tomography to mineral exploration: a case study from Siilinjärvi, Finland: Geophys. Prospect., 68, 254-269, https://doi.org/10.1111/1365-2478.12903, 2020.

Dunkin, J. W.: Computation of modal solutions in layerered, elastic mida at high frequencies, Bull. Seismol. Soc. Am., 55, 335-358, 1965.

380 Ekstrom, G., Tromp, J., and Larson, E. W. F.: Measurements and global models of surface wave propagation: J. Geophys. Res., 102, 8137–8157, https://doi.org/10.1029/96JB03729, 1997.

Fang, H., Yao, H., Zhang, H., Huang, Y., and van der Hilst, R. D.: Direct inversion of surface wave dispersion for three-dimensional shallow crustal structure based on ray tracing: methodology and application, Geophys. J. Int., 201, 1251-1263, https://doi.org/10.1093/gji/ggv080, 2015.

385 Gouédard, P., Yao, H., van der Hilst, R. D., and Verdel, A.: Surface-wave eikonal tomography in a scattering environment, SEG Technical Program Expanded Abstracts, 1919-1923, doi: 10.1190/1.3513217, 2010.

Haskell, N.: The dispersion of surface waves on multilayered media: Bul. Seimol. Soc. Am., 43, 17-34, https://doi.org/10.1785/BSSA0430010017, 1953.

Ikeda, T. and Tsuji, T.: Two-station continuous wavelet transform cross-coherence analysis for surface-wave tomography
390 using active-source seismic data, Geophysics, 85, EN17-EN28, https://doi.org/10.1190/geo2019-0054.1, 2020.

Kästle, E. D., El-Sharkawy, A., Boschi, L., Meier, T., Rosenberg, C., Bellahsen, N., Cristiano, L., and Weidle, C.: Surface wave tomography of the Alps using ambient-noise and earthquake phase velocity measurements, J. Geophys. Res.: Solid Earth, 123, 1770–1792, https://doi.org/10.1002/2017JB014698, 2018.

Khosro Anjom, F.: S-wave and P-wave velocity model estimation from surface waves, Ph.D. thesis, Politecnico di Torino,
395 2021.

Khosro Anjom, F., and Socco, L. V.: Improved surface wave tomography: Imposing wavelength-based weights, Extended Abstracts, 38th GNGTS national convention, 2019.

Kugler, S., Bohlen, T., Forbriger, T., Bussat, S., and Klein, G.: Scholte-wave tomography for shallow-water marine sediments, Geophys. J. Int., 168, 551–570, https://doi.org/10.1111/j.1365-246X.2006.03233.x, 2007.

Lin, F.-C., Moschetti, M. P., and Ritzwoller, M. H.: Surface wave tomography of the western United States from ambient seismic noise: Rayleigh and Love wave phase velocity maps, Geophys. J. Int., 173, 281–298, https://doi.org/10.1111/j.1365-246X.2008.03720.x, 2008.

Marquardt, D. W.: An algorithm for least squares estimation of nonlinear parameters, Journal of the Society of Industrial Applied Mathematics, 11(2), 431–441, https://doi.org/10.1137/0111030, 1963.

Noble, M., Gesret, A., and Belayouni, N.: Accurate 3-D finite difference computation of traveltimes in strongly heterogeneous media, Geophys. J. Int., 199, 422 1572-1585, https://doi.org/10.1093/gji/ggu358, 2014.

Papadopoulou, M.: Surface wave methods for mineral exploration, Ph.D. thesis, Politecnico di Torino, 2021.

Passier, M. L., Van der Hilst, R. D., and Snieder, R. K.: Surface wave waveform inversions for local shear-wave velocities under eastern Australia, Geophys. Res. Lett., 24, 1291-1294, https://doi.org/10.1029/97GL01272, 1997.

Picozzi, M., Parolai, S., Bindi, D., and Strollo, A.: Characterization of shallow geology by high-frequency seismic noise tomography, Geophys. J. Int., 176, 164–174, https://doi.org/10.1111/j.1365-246X.2008.03966.x, 2009.

Rector, J. W., Pfeiffe, J., Hodges, S., Kingman, J., and Sprott, E.: Tomographic imaging of surface waves: A case study from the Phoenix Mine, Battle Mountain, Nevada, The Leading Edge, 34, 1360-1364, https://doi.org/10.1190/tle34111360.1, 2015.

Ritzwoller, M. H. and Levshin, A. L.: Eurasian surface wave tomography: Group velocities, J. Geophys. Res.: Solid Earth, 103, 4839- 4878, https://doi.org/10.1029/97JB02622, 1998.

Rawlinson, N. and Sambridge, M.: Wave front evolution in strongly heterogeneous layered media using the fast marching method, Geophys. J. Int., 156, 631–647, https://doi.org/10.1111/j.1365-246X.2004.02153.x, 2004.

Shapiro, N. M., Ritzwoller, M. H., Molnar, P. and Levin, V.: Thinning and flow of Tibetan crust constrained by seismic anisotropy, Science, 305, 233–236, https://doi.org/10.1126/science.1098276, 2004.

Simons, F. J., Zielhuis, A., and van der Hilst, R. D.: The deep structure of the Australian continent from surface wave tomography, Develop. Geotect., 24, 17–43, https://doi.org/10.1016/S0419-0254(99)80003-2, 1999.

Spetzler, J., Trampert, J., and Snieder, R.: The effect of scattering in surface wave tomography, Geophys. J. Int., 149, 755-767, https://doi.org/10.1046/j.1365-246X.2002.01683.x, 2002.

Thomson, W. T.: Transmission of elastic waves through a stratified solid medium, J. appl. Geophys., 21, 89-93, https://doi.org/10.1063/1.1699629, 1950.

Trampert, J. and Spetzler, J.: Surface wave tomography: finite-frequency effects lost in the null space, Gephys. J. Int., 164, 394-400, https://doi.org/10.1111/j.1365-246X.2006.02864.x, 2006.

Trampert, J. and Woodhouse, J. H.: Global phase velocity maps of Love and Rayleigh waves between 40 and 150 seconds, Gephys. J. Int., 122, pp.675-690, https://doi.org/10.1111/j.1365-246X.1995.tb07019.x, 1995.

Van Heijst, H. J. and Woodhouse, J.: Global high-resolution phase velocity distributions of overtone and fundamental-mode surface waves determined by mode branch stripping, Geophys. J. Int., 137, pp.601-620, https://doi.org/10.1046/j.1365-246x.1999.00825.x, 1999.

Woodhouse, J. H. and Dziewonski, A. M.: Mapping the upper mantle: three-dimensional modelling of Earth structure by

435   inversion of seismic waveforms, J. Geophys. Res.: Solid Earth, 89, 5953– 5986, https://doi.org/10.1029/JB089iB07p05953,

1984.

Wu, Z. and Rector, J.: Seismic-velocity inversion using surface-wave tomography, SEG Technical Program Expanded

Abstracts, 2612-2616, https://doi.org/10.1190/segam2018-2998108.1, 2018.

Yao, H., Beghein, C., and van der Hilst, R. D.: Surface wave array tomography in SE Tibet from ambient seismic noise and

440   two-station analysis—II. Crustal and upper-mantle structure, Geophys. J. Int., 173, 205–219, https://doi.org/10.1111/j.1365-

246X.2007.03696.x, 2008.

Yao, H., van der Hilst, R. D., and Montagner, J.-P.: Heterogeneity and anisotropy of the lithosphere of SE Tibet from surface

wave array tomography, J. Geophys. Res.: Solid Earth (1978–2012), 115(B12), https://doi.org/10.1029/2009JB007142,

2010.

445   Yoshizawa, K. and Kennett, B. L. N.: Multimode surface wave tomography for the Australian region using a three-stage

approach   incorporating   finite   frequency   effects,   J.   Geophys.   Res.:   Solid   Earth,   109,   B02310,

https://doi.org/10.1029/2002JB002254, 2004.